Microwave Imaging of the Neck by Means of Artificial Neural Networks for Tumor Detection

CHIARA DACHENA [1], **ALESSANDRO FEDELI** [1] (Member, IEEE),

ALESSANDRO FANTI [2,3] (Member, IEEE), **MATTEO BRUNO LODI** [2] (Graduate Student Member, IEEE),

GIORGIO FUMERA [2] (Member, IEEE), **ANDREA RANDAZZO** [1] (Senior Member, IEEE),

AND MATTEO PASTORINO [1] (Fellow, IEEE)

[1] Department of Electrical, Electronic, Telecommunications Engineering, and Naval Architecture (DITEN), University of Genoa, 16145 Genoa, Italy

[2] Department of Electrical and Electronic Engineering, University of Cagliari, 09123 Cagliari, Italy

[3] Istituto Nazionale di Fisica Nucleare-CA, Complesso Universitario di Monserrato, 09042 Cagliari, Italy

CORRESPONDING AUTHORS: A. FEDELI AND A. FANTI (e-mail: alessandro.fedeli@unige.it; alessandro.fanti@unica.it)

This work was supported in part by the Artificial Intelligence in Medicine (AIM) Project under Grant INFN(CSN5).

ABSTRACT In this paper, a microwave imaging approach based on artificial neural networks (ANNs) for neck tumor detection is presented. The aim of this technique is to retrieve the geometric and dielectric properties of the neck to identify the possible presence of tumors, starting from scattered electric field data. A fully-connected neural network is developed to test the feasibility of the proposed approach. Moreover, a numerical model including the main features of a cross section of the neck is specifically designed in order to create a suitable training dataset. Subsequently, for the optimization of the ANN architecture and performance evaluation, a numerical analysis is conducted. A set of simulated cases, based on realistic neck phantoms, is tested to evaluate the robustness of the network. Preliminary results show the possibility to identify and locate neck tumors.

INDEX TERMS Microwave imaging, neck tumors, artificial neural networks, biomedical imaging, machine learning, inverse scattering.

I. INTRODUCTION

MICROWAVE imaging is a very promising technique for developing novel diagnostic tools in the medical field [1]. This method may offer several advantages over the other standard techniques, such as Magnetic Resonance Imaging (MRI), Computerized Tomography (CT) and projection radiography, since it does not require neither expensive apparatuses nor ionizing radiations. Moreover, a microwave imaging system can highlight additional details about the part of interest of the human body, which can be merged with the information obtained by the standard techniques. The use of microwave imaging is nowadays consolidated in some medical applications, like breast cancer [2]–[6] and brain stroke detection [7]–[10], although the application to other body parts is increasing, such as arms [11], torso [12], and neck [13], [14]. In addition to the neck imaging,

the last medical application is focused on the microwave hyperthermia of neck tumors [15]–[17]. Malignant primary and secondary cancers in the neck region, such as supra-glottic laryngeal carcinoma [18], thyroid cancer [19], cervical lymph node metastases [20], are frequently occurring, aggressive neoplasms with a 50% 5-year survival probability, which can be treated effectively by using microwave hyperthermia in synergy with radio- or chemotherapy [20]–[23]. However, to ensure a high-quality treatment and achieve an effective complete response, an accurate treatment planning phase, with numerical simulations, is required to choose the number, position and phases of the antennas [24], [25]. In this framework, the tumor localization and the retrieval of its electromagnetic properties through microwave imaging could facilitate the clinical setup and lead to an effective treatment [26], [27].

Microwave imaging is based on the acquisition of measurements due to the interactions between an incident electromagnetic radiation and the body under test [1]. The inversion procedure, to obtain the properties of the target starting from the scattered electric field data, requires the solution of an ill-posed and nonlinear electromagnetic problem [28]. To solve it, different methods were developed by using qualitative [29]–[32] or quantitative approaches [33]–[38]. In this framework, other new, fast and reliable non-linear approaches for addressing the imaging problem are investigated. In particular, artificial neural networks (ANNs) represent a recent and useful methodology for quantitative microwave imaging. The first applications of the ANNs were focused on shallow network architectures [39], [40]. In the last years, the use of deep Convolutional Neural Networks (CNNs) for solving the inverse problem has increased [41]–[47], and various CNN architecture were developed, such as U-net [48], ResNet [49] and VGG [50]. In addition, inversion techniques aimed at integrating physical insights into neural network architectures have also been proposed, with promising results [51], [52].

In this scenario, fully-connected neural networks represent an alternative approach for microwave imaging [53].

However, to retrieve the dielectric profile of the target, most of standard CNN-based architectures do not work directly with the measurements of scattered fields collected by the receiving antennas, but require a preliminary image retrieved by other techniques [41], [42], [45], [51], [54]. This image may be obtained with other inverse-scattering approaches, e.g., orthogonality sampling method (OSM) [55], back propagation (BP) [56] and direct sampling method [57].

In this paper, we present some preliminary results for the detection of neck tumors obtained by using ANNs applied to microwave imaging. To the best of the author's knowledge, this is the first time that a deep learning approach is used for neck tumor detection. As an initial evaluation, we used a fully-connected neural network, whose input is the scattered electric field, to reconstruct the geometric and dielectric properties of a cross section of the human neck with the aim of detecting the possible presence of neck tumors. It is worth remarking that, although the neck is a rather complicated structure with possible variations along the vertical direction (especially for what concerns the bone structure), several parts can be modeled, at least approximately, with cylindrical shapes. Consequently, in this initial work, we used a two-dimensional scalar scattering formulation involving only the cross-section of the neck, as often done in microwave imaging applications to reduce the required computational resources [58].

To obtain the dataset for the training phase, a strategy to create the neck phantoms is developed given the scarce availability of data [46]. The proposed strategy allows creating realistic neck phantoms in a simple and randomized way, varying the dielectric properties of the considered tissues
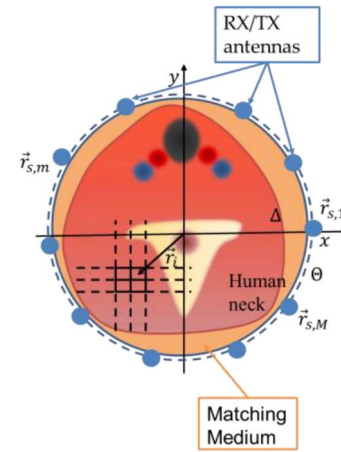

FIGURE 1. Configuration of the considered tomographic imaging problem for neck tumor detection.

and their geometry. In order to mimic neck tumors, circular shapes were taken into account, with different sizes and positions. Numerical analyses are firstly performed to select the best neural network architecture, varying the number of hidden layers and the number of neurons in each layer. After defining the network topology that exhibited the lowest reconstructions errors, this is used to test different simulated cases with realistic neck phantoms, some with tumor and some without.

This paper is organized as follows. Section II reports the formulation of electromagnetic inverse scattering problem, introducing the network architecture. In Section III, the training set preparation is explained. Preliminary numerical results are shown in Section IV. Conclusions follow.

II. FORMULATION OF THE IMAGING METHOD
A. ELECTROMAGNETIC FORMULATION
The considered two-dimensional geometry is shown in Fig. 1. N antennas are located around the neck and are modeled as z-directed line current sources located at points $\vec{r}_s$, $s = 1, \ldots, S$. Each antenna sequentially illuminates the neck with a transverse-magnetic (TM) field and the total electric field due to the interaction with the neck is collected in a measurement domain Θ composed, for each transmitting antenna, by the remaining at $M = N - 1$ antennas, modeled as ideal probes located at points $\vec{r}_{s,m}$, $m = 1, \ldots, M$. Moreover, the field data are collected for F different frequencies in a band B.

In general, to reconstruct the relative dielectric permittivity ε_r and the electric conductivity σ of a cross section of the neck, an inverse scattering problem has to be solved. For the sake of simplicity, a single-view and single-frequency case is described here. In what follows, the indexes $s = 1, \ldots, S$ and $f = 1, \ldots, F$ will represent the considered view and frequency, respectively. As shown in Fig. 1, the investigation domain Δ (*i.e.*, the circular region of interest where the cross section of the neck is assumed to lie) is partitioned into I square subdomains R_i, centered at $\vec{r}_i$, $i = 1, \ldots, I$,

with side length ρ. With this assumption, the samples of the z-component of the electric field due to the scattering phenomena in the measurement domain, which are contained in the array $\boldsymbol{\psi}_{scatt}^{s,f} = [\psi_{scatt}^{s,f(1)}, \ldots, \psi_{scatt}^{s,f(M)}]^{\mathrm{T}} = \boldsymbol{\psi}_{tot,ext}^{s,f} - \boldsymbol{\psi}_{ref,ext}^{s,f}$, being $\boldsymbol{\psi}_{tot,ext}^{s,f}$ and $\boldsymbol{\psi}_{ref,ext}^{s,f}$ the corresponding arrays of the total and reference electric fields, are related to the dielectric properties of the target by means of the following equations [28]:

$$\boldsymbol{\psi}_{tot}^{s,f} = \boldsymbol{\psi}_{ref}^{s,f} + \mathbf{g}_{state}^{f}\mathrm{diag}(\boldsymbol{\chi})\boldsymbol{\psi}_{tot}^{s,f} \tag{1}$$

$$\boldsymbol{\psi}_{scatt}^{s,f} = \mathbf{g}_{data}^{s,f}\mathrm{diag}(\boldsymbol{\chi})\boldsymbol{\psi}_{tot}^{s,f} \tag{2}$$

where $\boldsymbol{\psi}_{ref}^{s,f} = [\psi_{ref}^{s,f(1)}, \ldots, \psi_{ref}^{s,f(I)}]^{\mathrm{T}}$ and $\boldsymbol{\psi}_{tot}^{s,f} = [\psi_{tot}^{s,f(1)}, \ldots, \psi_{tot}^{s,f(I)}]^{\mathrm{T}}$ are the arrays containing the z-component of the reference and total electric fields for the sth view and the fth frequency in the investigation domain. The reference field is due to a given reference configuration when illuminated by the incident electromagnetic field produced by the source, which is modeled as a homogeneous circular cylinder with the same dimension of the investigation domain and the same dielectric properties of the matching medium. The $\mathbf{g}_{state}^{f}$ and $\mathbf{g}_{data}^{s,f}$ matrices contain the integrals of the inhomogeneous Green's function for the reference configuration [28]. Finally, the array of the contrast function $\boldsymbol{\chi} = [\frac{\varepsilon(\vec{r}_1)-\varepsilon_{ref}(\vec{r}_1)}{\varepsilon_b}, \ldots, \frac{\varepsilon(\vec{r}_I)-\varepsilon_{ref}(\vec{r}_I)}{\varepsilon_b}]$ contains the values of the complex dielectric permittivity of the actual and reference configurations in each subdomain of Δ. Combining (1) and (2), the following equation describing the whole electromagnetic scattering phenomena is defined:

$$\boldsymbol{\psi}_{scatt}^{s,f} = \mathbf{g}_{data}^{s,f}\mathrm{diag}(\boldsymbol{\chi})\Big[\mathbf{I} - \mathbf{g}_{state}^{f}\mathrm{diag}(\boldsymbol{\chi})\Big]^{-1}\boldsymbol{\psi}_{ref}^{s,f} \tag{3}$$

where $\mathbf{I}$ is an $I \times I$ identity matrix.

The aim of this paper is to invert such a nonlinear relationship with an ANN architecture in order to retrieve the dielectric properties of the actual configuration ε_r and σ. The real and imaginary parts of the scattered electric fields are the input data for the considered neural network.

B. NETWORK ARCHITECTURE

To reconstruct the dielectric properties of the neck starting from scattered electric fields, a feed-forward fully-connected network is proposed in this study. This kind of network allows implementing a direct inversion from the scattered electric field to the dielectric properties of the neck profiles.

The adopted fully-connected network is reported in Fig. 2. All the hidden layers have the same number of units. The network input is the array of scattered electric fields $\mathbf{P} = [Re\{\boldsymbol{\psi}_{scatt}^{1,1}\}^T, \ldots, Re\{\boldsymbol{\psi}_{scatt}^{S,F}\}^T, Im\{\boldsymbol{\psi}_{scatt}^{1,1}\}^T, \ldots, Im\{\boldsymbol{\psi}_{scatt}^{S,F}\}]^T$ which contains the real and imaginary part of the scattered field for each view s and frequency f. The output of the network is an array containing the values of the dielectric properties in each cell R_i of the investigation domain $\mathbf{O} = [\varepsilon_r(\vec{r}_1), \ldots, \varepsilon_r(\vec{r}_I), \sigma(\vec{r}_1), \ldots, \sigma(\vec{r}_I)]^T$.
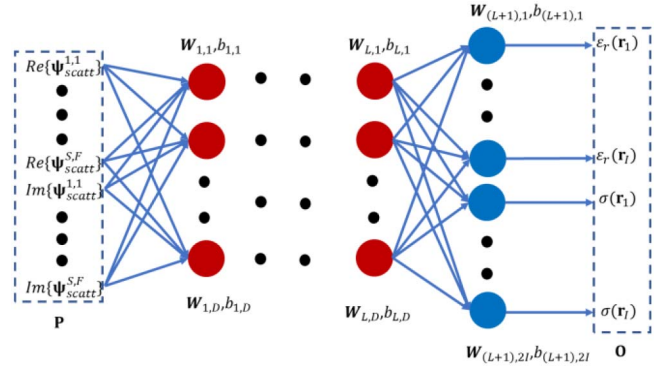

FIGURE 2. Sketch of the adopted fully-connected ANN architecture.

For the dth unit of the lth layer of the fully-connected network, a vector of weights of its input connections $\mathbf{W}_{l,d} \in \mathbb{R}^D$ and a scalar bias $b_{l,d}$ are defined, with $l = 1, \ldots, L$ and $d = 1, \ldots, D$ that represent the number of hidden layers and neurons for each layer, respectively. The last layer, here denoted as $L + 1$, presents a different number of neurons equal to $2I$, where I is defined in Section II-A. The output array $\mathbf{O}$ is obtained as:

$$\mathbf{O} = \mathbf{R}\big[\mathbf{W}_{L+1,1}^{\mathrm{T}}\mathbf{O}_L + b_{L+1,1}, \ldots, \mathbf{W}_{L+1,2I}^{\mathrm{T}}\mathbf{O}_L + b_{L+1,2I}\big]^{\mathrm{T}} \tag{4}$$

with $\mathbf{W}_{L+1,d}^{\mathrm{T}} \in \mathbb{R}^{2I}$ and $b_{L+1,d} \in \mathbb{R}$. The output of a generic layer $l = 2, \ldots, L$ can be written as:

$$\mathbf{O}_l = \mathbf{R}\big[\mathbf{W}_{l,1}^{\mathrm{T}}\mathbf{O}_{l-1} + b_{l,1}, \ldots, \mathbf{W}_{l,D}^{\mathrm{T}}\mathbf{O}_{l-1} + b_{l,D}\big]^{\mathrm{T}} \tag{5}$$

For the first hidden layer, $l = 1$, the output is:

$$\mathbf{O}_1 = \mathbf{R}[\mathbf{W}_{1,1}^{\mathrm{T}}\mathbf{P} + b_{1,1}, \ldots, \mathbf{W}_{1,D}^{\mathrm{T}}\mathbf{P} + b_{1,D}]^{\mathrm{T}} \tag{6}$$

with $\mathbf{W}_{1,d}^{\mathrm{T}} \in \mathbb{R}^{S \times F \times M}$ and $b_{1,d} \in \mathbb{R}$, where the vector $\mathbf{P}$ represents the input of the neural network. In the previous equations, the term $\mathbf{R}$ denotes the Rectified Linear Unit (ReLu) activation function [59], *i.e.*,

$$\mathbf{R}(\mathbf{x}) = [\mathrm{relu}(x_1), \mathrm{relu}(x_2), \ldots, \mathrm{relu}(x_D)]^{\mathrm{T}} \tag{7}$$

where $\mathbf{x} = [x_1, x_2, \ldots, x_D]^T$ and

$$\mathrm{relu}(x) = \begin{cases} x, & if \ x \geq 0 \\ 0, & otherwise \end{cases} \tag{8}$$

Finally, the ADAM optimization method [60] is used for the updating rule for the training phase, to minimize the loss function, which is calculated as:

$$\Lambda = \mathrm{E}_{\varepsilon_r} + \mathrm{E}_{\sigma} \tag{9}$$

where the normalized root mean square errors $\mathrm{E}_{\varepsilon_r}$ and E_{σ} are given by:

$$\mathrm{E}_{\varepsilon_r} = \frac{\|\boldsymbol{\varepsilon}_{r,rec} - \boldsymbol{\varepsilon}_{r,real}\|^2}{\|\boldsymbol{\varepsilon}_{r,real}\|^2} \tag{10}$$

$$\mathrm{E}_{\sigma} = \frac{\|\boldsymbol{\sigma}_{rec} - \boldsymbol{\sigma}_{real}\|^2}{\|\boldsymbol{\sigma}_{real}\|^2} \tag{11}$$
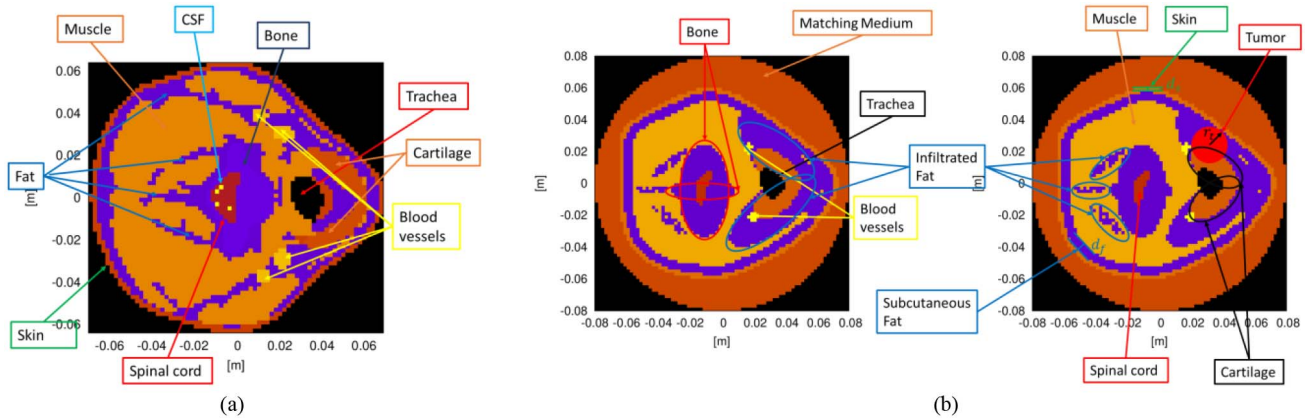
FIGURE 3. Realistic cross section of the neck: (a) Slice extracted from the *Duke* man phantom of the *Virtual Family*. (b) Created phantom with simplified anatomical structures.

with $\boldsymbol{\varepsilon}_{r,rec} = [\varepsilon_{r,rec}(\vec{r}_1), \ldots, \varepsilon_{r,rec}(\vec{r}_I)]$ and $\boldsymbol{\varepsilon}_{r,real} = [\varepsilon_{r,real}(\vec{r}_1), \ldots, \varepsilon_{r,real}(\vec{r}_I)]$ representing the array of relative dielectric permittivity of the reconstructed and actual cross section of the neck, respectively. In the same way, $\boldsymbol{\sigma}_{rec}$ and $\boldsymbol{\sigma}_{real}$ constitute the arrays of electric conductivity.

It is worth noting that, although (1) and (2) are not explicitly used at the input layer of the present fully-connected architecture, connections can be established between ANN architectures with fully-connected layers and iterative methods for nonlinear electromagnetic inverse scattering problems, where the number of layers of the network becomes linked with number of iterations of conventional solving procedures [61]. As a result, among the various alternative solutions, the direct use of neural networks offers an efficient alternative to solve the nonlinear problem at hand. In the present application, the proposed ANN architecture has been selected due to its very good balance between simplicity and accuracy of reconstruction results.

III. DEFINITION OF THE TRAINING SET

In order to perform a quantitative inversion by means of the proposed neural network, a strategy to define the training set is developed with the aim of creating a set of "virtual" neck phantoms, given that there is an established lack of datasets for electromagnetic problems dealing with machine learning [46]. The strategy to obtain a cross section of the neck is based on a realistic neck slice extracted from the *Duke* man phantom of the *Virtual Family* [62]. The extraction procedure and the following process to obtain neck phantoms are performed in MATLAB R2020a (The MathWorks, Natick, MA, USA) and allow obtaining a reference slice stored as a matrix in ASCII format. The considered slice from the *Duke* phantom is extracted at 1.60 m of height and includes the third cervical vertebra, as shown in Fig. 3(a). The discretization of the considered slice is equal to 2 mm and 9 biological tissues are present, *i.e.*, skin, fat, muscle, vertebral bone, spinal cord, trachea, cartilage, cerebrospinal fluid (CSF) and blood vessels. To obtain a suitable phantom that can mimic the real one, all tissues are considered, except CSF, which is only present in a few pixels of the slice,

as can be seen in Fig. 3(b). The remaining tissues, which are fundamental to obtain a realistic cross section of the neck, are modeled in a simple way to allow a reproducible and randomized generation of phantoms. In this case, the boundaries of tissues are modeled by means of two different approaches: ellipses and splines. As shown in Fig. 3(b), the tissues boundaries modeled with ellipses are:

- Vertebral Bone
- Infiltrated Fat
- Cartilage.

Spline functions are used to model the remaining biological tissues boundaries, *i.e.*:

- Skin
- Subcutaneous Fat
- Muscle
- Spinal Cord
- Blood Vessels
- Trachea.

Considering all tissues, those created with ellipses and those with the spline functions, the obtained phantom – although unavoidably simplified – reproduces in a suitable way the cross section of the neck. To create the training set, a huge number (hundreds) of neck phantoms are required. For this reason, each geometrical parameter, *i.e.*, center and semi-axes of ellipses, coordinates of the spline control points (as detailed in Sections III-A and III-B) and dielectric properties, randomly varies in a certain range to obtain different phantoms preserving the simplicity and the realism of the neck. The ranges in which the dielectric properties vary are selected following their dielectric behavior in the considered frequency band [63]. The coordinates of the control points vary along the x-y axis, both in the negative and positive directions. Moreover, each neck structure is rotated by applying a rotation matrix with random angle $\theta \in [-45°, 45°]$, to increase the variability of the training set. In Table 1, the properties of the tissues considered for the developed phantoms are given. The value of each parameter is randomly defined (with uniform distribution in the reported intervals)

TABLE 1. Parameters of the tissues inside the neck phantoms.

Neck tissue	Developed phantom			No. of control points	Variability of semi-axis a, b [mm]	Variability of ellipses center (x_0, y_0) [mm]	Rotation angle α [deg]	Variability of control points [mm]	ε_r	σ [S/m]
Skin	Spline			14	–	–	–	$[-6, 6]$	$[40, 50]$	$[0.6, 1]$
Fat	Subcutaneous	Spline		14	–	–	–	$[-6, 6]$	$[8, 15]$	$[0.06, 0.13]$
	Infiltrated	Filled Ellipses	Fat 1	–	$a \in [10, 16]$ $b \in [26, 40]$	$x_0 \in [20, 34]$ $y_0 \in [4, 14]$	$[215, 235]$	–		
			Fat 2		$a \in [10, 16]$ $b \in [26, 40]$	$x_0 \in [20, 34]$ $y_0 \in [-14, -4]$	$[125, 145]$			
		Partially Filled Ellipses	Fat 3	–	$a \in [2, 6]$ $b \in [8, 16]$	$x_0 \in [-14, 6]$ $y_0 \in [-6, 6]$	$[215, 235]$	–		
			Fat 4		$a \in [2, 6]$ $b \in [8, 16]$	$x_0 \in [-14, 6]$ $y_0 \in [-6, 6]$	$[125, 145]$			
			Fat 5		$a \in [2, 6]$ $b \in [6, 14]$	$x_0 \in [-14, 6]$ $y_0 \in [-6, 6]$	0			
Muscle	Spline			14	–	–	–	$[-6, 6]$	$[50, 60]$	$[0.7, 1]$
Bone	Ellipses	Bone 1		–	$a \in [20, 32]$ $b \in [6, 20]$	$x_0 \in [-14, 6]$ $y_0 \in [-6, 6]$	0	–	$[10, 20]$	$[0.06, 0.2]$
		Bone 2			$a \in [6, 20]$ $b \in [20, 32]$	$x_0 \in [-14, 6]$ $y_0 \in [-6, 6]$	0			
Cartilage	Ellipses	Cartilage 1		–	$a \in [6, 10]$ $b \in [20, 30]$	$x_0 \in [20, 34]$ $y_0 \in [4, 10]$	$[215, 235]$	–	$[44, 49]$	$[0.5, 0.8]$
		Cartilage 2			$a \in [6, 10]$ $b \in [20, 30]$	$x_0 \in [-34, -20]$ $y_0 \in [4, 10]$	$[125, 145]$			
Spinal Cord	Spline			5	–	–	–	$[-2, 4]$	$[30, 40]$	$[0.4, 0.7]$
Blood Vessels	Spline			4	–	–	–	$[-2, 2]$	$[58, 68]$	$[1.3, 1.6]$
Trachea	Spline			5	–	–	–	$[-2, 2]$	1	0
CSF	–			–	–	–	–	–		–
Tumor	Ellipse			–	$a = b \in [5, 15]$	$x_0 \in [x_0^{trachea} + 10, x_0^{trachea} + 20]$ $y_0 \in [y_0^{trachea} - 10, y_0^{trachea} + 10]$	0	–	$[55, 65]$	$[0.5, 1]$

and independent from each other. The approach used to generate each tissue region, the variability of the center position and the size of semi-axes for ellipses, the number of control points and their variability for the spline functions, as well as the variability of the dielectric properties are also provided.

Finally, to obtain the neck cross section with tumor (*i.e.*, to reproduce a pathological situation) a circle with radius r_t is inserted in the anterior part of the neck, near the trachea. In these kinds of tumors, *i.e.*, supraglottic laryngeal carcinoma [18] and thyroid cancer [19], the cross section can be approximated as a circular inclusion [64]. Also in previous works [65]–[67], the tumor is simulated like a circle. Tumors such as thyroid cancers [18], [64], neck sarcomas or cervical lymph node metastases [20] are nodular, being approximately spherical, with a radius in the range 3-5 mm, located up to 3 cm below the skin surface [68]–[70]. To reproduce in an accurate way the dielectric properties of the tumor, the results obtained in [66] are followed. For most neck tumors, the relative dielectric properties are relatively high, and in the considered frequency band are on average around $\varepsilon_r \approx 59$ and $\sigma \approx 0.9$ [S/m], depending on the type and staging, as can be derived by MRI and as usually modeled in numerical studies in the field of microwave hyperthermia [14], [17], [65], [67]. For this reason, by also taking into account a possible variability of such parameters, the dielectric properties of the simulated tumor model were

chosen in the range between 55 and 65 for the relative dielectric permittivity, whilst the electrical conductivity lies within [0.5, 1] S/m.

At the end, the generated neck phantom is set inside a circular shape with radius $r = 8$ cm, representing the matching medium, between the antenna and the neck. The dielectric properties of the matching medium have been selected in order to increase the field penetration and to reduce the reflection due to the skin. In particular, as shown in [13], a 70% glycerin/water mixture allows obtaining a good trade-off between these two requirements. Consequently, in this work the dielectric properties of the matching medium have been set to $\varepsilon_r = 43$ and $\sigma = 0.8$ S/m, *i.e.*, an average value of such a mixture in the considered frequency band.

A. TISSUES MODELED WITH NATURAL CUBIC SPLINE FUNCTION

As previously mentioned, in order to define a curve that models the particular shape of some tissue boundaries, the natural cubic spline functions are considered. This kind of functions takes the coordinates of some chosen points, called *control points*, and defines a curve that passes through them. In this way, a specific shape is obtained. Given a set of control points in x- and y- coordinates, a two-dimensional curve is written parametrically as [71]:

$$\mathbf{r}_{spline}(t) = \left(x_{spline}(t), y_{spline}(t) \right) \tag{12}$$
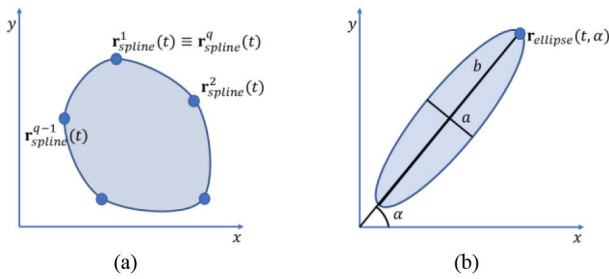
FIGURE 4. Sketch of (a) spline curve and (b) ellipse generation.

where $x_{spline}(t)$ and $y_{spline}(t)$ are single-valued functions of the parameter t of a point on the curve for any value of t [71]. The curve is split into q sections, each defined by separate polynomials to form a piecewise polynomial curve, as shown in Fig. 4(a). In general, the x-coordinates $x_{spline}(t)$ of points on a curve are determined only by the x-coordinates of the control points, analogously to $y_{spline}(t)$. Since both $x_{spline}(t)$ and $y_{spline}(t)$ are treated in the same way, we will discuss only $x_{spline}(t)$. The essential idea is to fit a piecewise function with a third-degree polynomial defined by [71]:

$$x_{spline}^i(t) = a_i t^3 + b_i t^2 + c_i t + e_i \qquad (13)$$

for $i = 1, 2, \ldots, q-1$. To determine the $4(q-1)$ coefficients that completely determine a particular polynomial, constraints are needed. In particular, it is required that the piecewise function $x_{spline}^i(t)$ interpolates all data points, for $i = 1, \ldots, q-1$, and it is necessary that $x_{spline}^i(t)$, with its first and second derivative, are continuous in the interval $[t_1, t_q]$ for $i = 1, \ldots, q-1$. The coefficients a_i, b_i, c_i and e_i can be obtained explicitly for each interval as described in [72]. Finally, the definition of *natural* means that the second derivative will be equal to zero at the endpoints [71].

With this approach, the first modeled tissue boundary is the skin, which also defines the external shape of the neck. To develop the skin structure, 14 control points are considered adequate to mimic the external shape of the phantom. The control points allow generating different configurations and sizes of the neck. As shown in Fig. 3(b), the obtained external shape is similar to the actual one. The thickness of the skin, d_s, vary in the range [2, 4] mm. After that, the subcutaneous fat tissue is also modeled with spline functions. As reported in Fig. 3(b), this tissue is located internally, adjacent to the skin and its thickness d_f varies between [2, 8] mm [64]. The subcutaneous fat is located along the skin, both in the anterior and posterior part of the neck. Defined these two tissues (skin and subcutaneous fat) the structure is internally filled with the dielectric properties of muscle. In this way, the shape of muscle depends only on the thickness of skin and subcutaneous fat. Then, the remaining anatomical structures are located inside the neck, overlapping with the previous ones already created.

Internally to the vertebral bone, as shown in Fig. 3(b), the spinal cord is inserted. In this case, 5 control points are used to define the tissue and are chosen to obtain a shape that

can mimic the stretched configuration of the spinal cord. Other considered structures are the blood vessels. In the *Virtual Family* phantom [Fig. 3(a)], there are two arteries and two veins, one for each side of the neck. In the developed phantom, only one vessel for each side is considered for simplicity and because their presence is not so relevant for this study. In this case, 4 control points are used to define the shape of the vessel, and then such a shape is duplicated to obtain the second vessel [Fig. 3(b)]. Finally, the trachea structure is created. Here, 5 control points are used to obtain the structure. As shown in Fig. 3(b), the trachea is embedded inside the cartilage tissue.

B. TISSUES MODELED WITH ELLIPSES
To reproduce other tissue structures, one or more ellipses are used. These curves can be defined in parametric form as:

$$x_{ellipse}(t, \alpha) = x_0 + a \cos(t) \cos(\alpha) - b \sin(t) \sin(\alpha)$$
$$y_{ellipse}(t, \alpha) = y_0 + b \sin(t) \cos(\alpha) + a \cos(t) \sin(\alpha) \quad (14)$$

where x and y are the coordinates of any point on the ellipse, x_0 and y_0 are the coordinates of the ellipse center, a and b are the semi-axes along the x- and y-directions, respectively, t is the parameter $\in [0, 2\pi]$ and α is the rotation angle, as illustrated in Fig. 4(b).

First, the vertebral bone is created using two ellipses, one placed vertically and the other horizontally. Another tissue modeled with elliptic shape is the infiltrated fat. For this tissue, three ellipses are placed near the bone, in the posterior region of the neck. Within such ellipses, a binary random variable with uniform distribution defines whether pixels are occupied by fat or not. To complete the presence of fat in the phantom, other two ellipses are defined, which are placed in the anterior part of the neck. The last biological tissue modeled with elliptic structures is cartilage: two ellipses are located in the anterior part of the neck, overlapped to the fat structure. To increment the variability of the biological tissues, the centers and the semi-axes of each ellipse are allowed to vary in the ranges defined in Table 1.

IV. PRELIMINARY RESULTS
A preliminary analysis is performed in order to choose the best parameters for the neural network architecture. Then, the selected architecture is tested with different cases.

To train the developed neural network, a data set of 30, 000 simplified neck phantoms is built. Each neck phantom is generated by the random variations of the dielectric and geometrical properties described in Section III. The dataset does not contain any duplicate. The investigation domain is discretized with $I = 5024$ square cells of side 2 mm. Half of the dataset represents the neck profile with the presence of variable tumors in the anterior neck area, whereas the other half is without tumor. This dataset is portioned into two subsets: 95% of the samples for the training procedure and the remaining 5% for the validation phase. A custom direct solver based on method of moments (MoM) is applied

on the created neck profiles to calculate the corresponding scattered electric fields, with $F = 7$ frequencies in the range [600, 900] MHz, $S = 10$ antennas, and $M = 9$ measurement points. Moreover, a white Gaussian noise with zero mean value and a signal-to-noise ratio (SNR) of 35 dB has been added to the total electric fields of validation cases to obtain more realistic data.

The neural network training starts with an initial bias equal to zero and weight parameters are initialized by a Gaussian distribution with zero mean value and standard deviation set to 10^{-2}. A constant L^2 norm regularization parameter equal to 10^{-4} is adopted, to avoid overfitting, and the ADAM method is used to minimize the loss function, with an initial learning rate of 10^{-3} and 500 epochs for each training phase, with mini-batch size of 256. The input layer size is defined as $F \times S \times M \times 2 = 1260$, whereas the output layer consists of $2I = 10048$ neurons.

A. SELECTION OF THE NETWORK ARCHITECTURE PARAMETERS

In order to find a trade-off between the accuracy in the reconstruction and computational complexity, different network architectures are tested. To perform a quantitative assessment for evaluating the best architecture, for each proposed network structure, the average error parameters E_{ε_r} and E_σ described in (10) and (11) are calculated for the reconstructions of the data in the validation set.

In this analysis, the impact of the number of hidden layers and the number of neurons (nodes) are evaluated. To this end, the number of hidden layers is set to $L = \{1, 2, \ldots, 5\}$, whereas the number of neurons for each layer is $D = \{32, 64, 96, \ldots, 512\}$. Fig. 5, which reports the behaviors of E_{ε_r} and E_σ versus L and D, shows that for $L = 5$ hidden layers and $D = 448$ neurons the smallest reconstruction errors are obtained, both for relative dielectric permittivity E_{ε_r} [Fig. 5(a)] and for electric conductivity E_σ [Fig. 5(b)]. The findings show that E_{ε_r} and E_σ assume the highest values for $L = 1$, regardless of the value of D. Moreover, the reconstruction errors remain high for $L = 32$ and any value of D. This analysis highlights that for one hidden layer and a low number of neurons the reconstruction is not accurate. Indeed, as shown in other works [53], a too small number of hidden layers and neurons does not allow a good quality of the recovery.

Following this preliminary analysis, quantitative reconstructions of the cross section of neck are analyzed with different values of L and D. In particular, three different network topologies are tested against two selected cases from the validation set.

The actual values of the relative dielectric permittivity and electric conductivity in the first case are shown in Fig. 6(a) and Fig. 6(e), respectively. The neck cross section, in this configuration, presents each biological tissue in a normal physiological condition, without any tumor. To evaluate the capability of retrieving the distributions of the dielectric properties, the first tested network topology presents
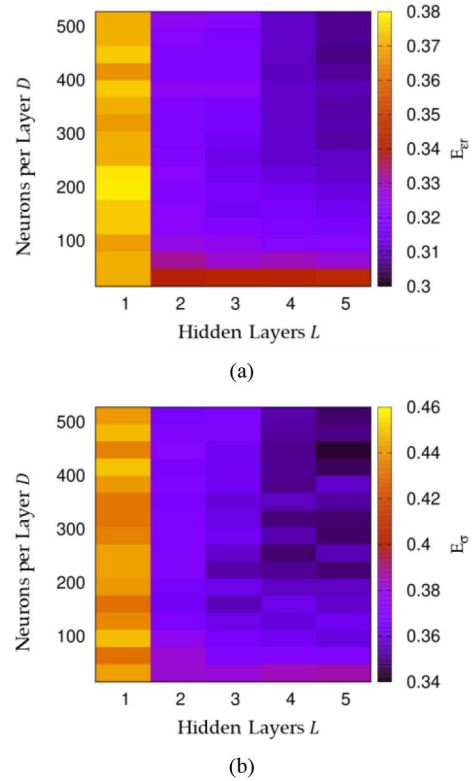

FIGURE 5. Mean reconstruction error on (a) ε_r and (b) σ versus the number of hidden layers and neurons per layer.

$L = 1$ and $D = 32$ (*i.e.*, the simplest network architecture). Fig. 6(b)–(f) report the reconstructed maps of the relative dielectric permittivity and of the electric conductivity, which are not very accurate in this case. Indeed, the relative dielectric permittivity value of the infiltrated fat near the cartilage is overestimated (24-32 *vs.* the actual values of 8-15), the blood vessels are not well detected, and the subcutaneous fat thickness is larger than in the actual configuration. The same considerations hold for the electric conductivity reconstruction. The second tested network topology presents $L = 3$ and $D = 224$, a slightly more complex neural network structure. The reconstructions obtained with this network are shown in Fig. 6(c)–(g). Now, the reconstructions are more precise: the thickness of the subcutaneous fat is close to its true value for both ε_r and σ; the cartilage is better shaped, and the trachea is well retrieved. On the other hand, the reconstructions show some artefacts outside the neck, in the matching medium, and in the relative dielectric permittivity overall. The last considered neural network has $L = 5$ and $D = 448$, and it shows the best results of the E_{ε_r} and E_σ errors. The reconstructed maps of the relative dielectric permittivity and electric conductivity are plotted in Fig. 6(d) and Fig. 6(h). With this network architecture, the reconstructions are better than those obtained with the previous topologies. Here, in both reconstructions of ε_r and σ, the blood vessels are well identified, the cartilage shape reproduces well the real one and the thickness of the subcutaneous fat is reconstructed
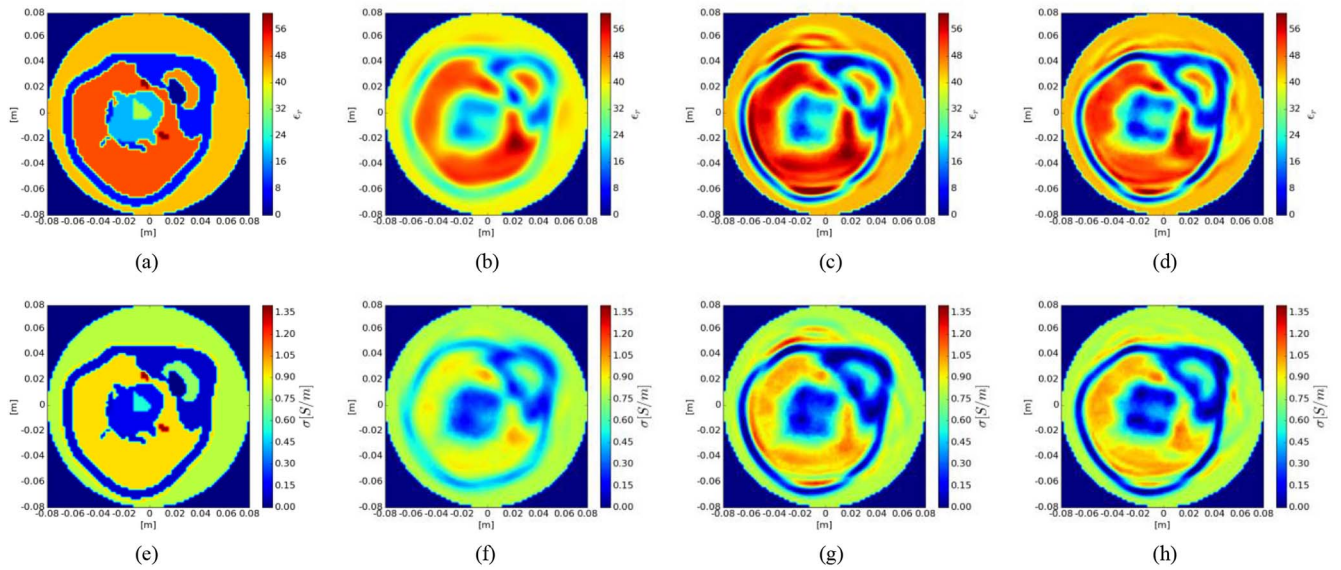
FIGURE 6. Neck configuration without tumor, validation set: (a) Actual relative dielectric permittivity. Reconstruction of relative dielectric permittivity with (b) $L = 1$ and $D = 32$; (c) $L = 3$ and $D = 224$; (d) $L = 5$ and $D = 448$. (e) Actual electric conductivity. Reconstruction of electric conductivity with (f) $L = 1$ and $D = 32$; (g) $L = 3$ and $D = 224$; (h) $L = 5$ and $D = 448$.
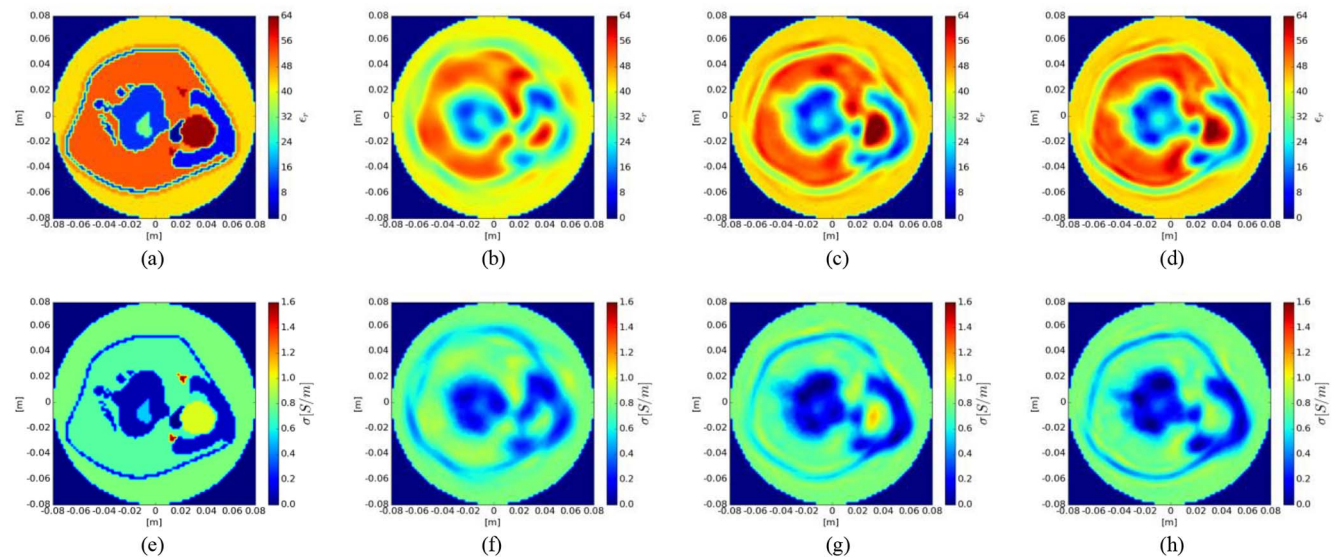

FIGURE 7. Neck configuration with tumor, validation set: (a) Actual relative dielectric permittivity. Reconstruction of relative dielectric permittivity with (b) $L = 1$ and $D = 32$; (c) $L = 3$ and $D = 224$; (d) $L = 5$ and $D = 448$. (e) Actual electric conductivity. Reconstruction of electric conductivity with (f) $L = 1$ and $D = 32$; (g) $L = 3$ and $D = 224$; (h) $L = 5$ and $D = 448$.

correctly. Moreover, the spinal cord shape is detected, and the artifacts visible in the previous reconstructions are less evident.

To test the ability to detect the presence of a tumor, a second case extracted from the validation set is analyzed. This case is a cross section of the neck with a tumor in the anterior neck part, as shown in Fig. 7(a)–(e). In this configuration, too, the reconstructions are evaluated for three different network architectures, as explained previously. For the first neural network, Fig. 7(b)–(f) report the reconstructed maps of the dielectric properties ε_r and σ. As before, the reconstructions are not very precise, with an overestimation of

subcutaneous fat thickness, the absence of blood vessels, and an incorrect tumor shape. The reconstructions achieved with the second neural network, as can be seen in Fig. 7(c)–(g), highlight a significant improvement of results. The tumor is better reconstructed, as well as fat, both for dielectric and geometric properties. Finally, the last neural network is tested, with $L = 5$ and $D = 448$, and the corresponding reconstructions can be found in Fig. 7(d)–(h). Now, the external shape of the neck is better retrieved than in the previous cases [Fig. 7(b), (c), (f), (g)]. Moreover, the tumor is identified with its correct shape and the cartilage around it is identified correctly. The trachea is now detected, although
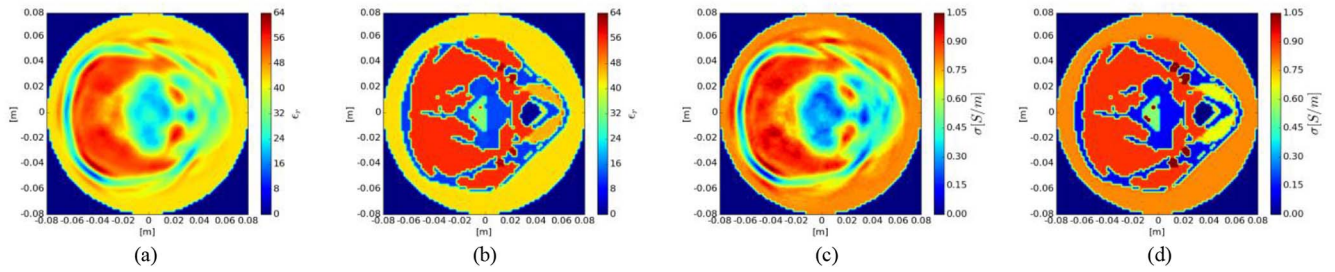
FIGURE 8. Realistic neck configuration without tumor (Test case #1). Relative dielectric permittivity: (a) Reconstructed values; (b) Actual configuration. Electric conductivity: (c) Reconstructed values; (d) Actual configuration.
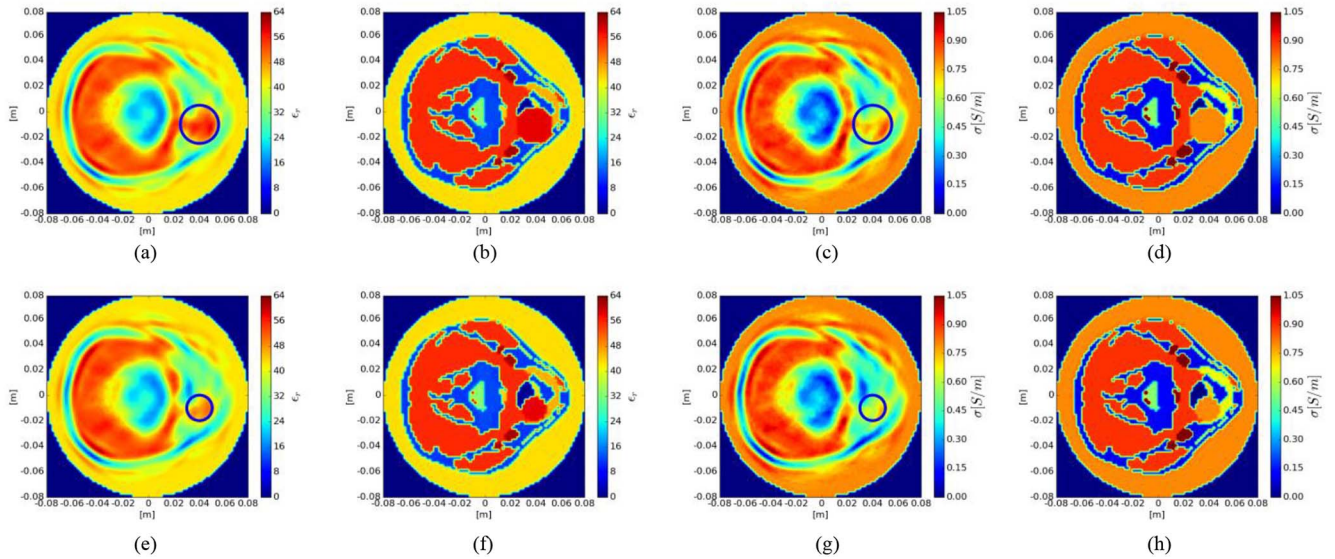

FIGURE 9. Realistic neck configuration with tumor centered in $(0.04, -0.01)$ m. Test case #2, tumor radius $r_t = 1.5$ cm: (a) Reconstructed and (b) actual relative dielectric permittivity; (c) Reconstructed and (d) actual electric conductivity. Test case #3, tumor radius $r_t = 1$ cm: (e) Reconstructed and (f) actual relative dielectric permittivity; (g) Reconstructed and (h) actual electric conductivity.

the dielectric permittivity is overestimated and assumes values similar to those of the fat. However, this fact does not prevent the identification of the tumor. Moreover, the spinal cord is properly recognized inside the vertebral bone, too, both in the relative dielectric permittivity and electric conductivity (*e.g.,* estimated values of 25-35 *vs.* the actual values of 30-40). It is worth noting that in general, the dielectric properties of the muscle and tumor tissues may overlap. However, the considered laryngeal tumors are usually located in the anterior part of the neck and near the cartilage, where there is a reduced presence of muscle tissue. In this case, it is still possible to identify the presence of anomalies/tumors in reconstructed images, as confirmed by Fig. 7.

After this preliminary analysis, a network with $L = 5$ hidden layers and $D = 448$ neurons has been selected for the training procedure and to test different cases with and without tumor.

B. QUANTITATIVE RECONSTRUCTION OF TEST CASES
To prove the robustness of the approach, the identified network is tested on realistic numerical neck phantoms extracted from the *Virtual Family* [62]. Five test cases

are created to assess the capability of discriminating the presence, size and position of the tumor. The dielectric properties of neck tissues are related to the frequency of 750 MHz, and the tumor properties are set to $\varepsilon_r = 58$ and $\sigma = 0.8$ [S/m], according to [66], [73].

First, a case without tumor is considered, to check the ability to reconstruct the dielectric properties in a healthy situation (Test case #1). Fig. 8(a)–(c) represent the reconstructions of the relative dielectric permittivity and the electric conductivity, respectively. The actual configurations related to such a case are presented in Fig. 8(b)–(d). In the map of ε_r, the neural network is able to detect the vertebral bone, the spinal cord inside it, as well as the external shape of the neck. Moreover, in the reconstruction of the electric conductivity, the trachea is quite well detected. In both reconstructions the absence of tumor is verified. Successively, four cases with tumor-like inclusions are tested. Two different dimensions of the tumor, with the same center, are evaluated. In the first configuration (Test case #2), a circular target of radius equal to $r_t = 1.5$ cm representing the tumor was included. Fig. 9(a) and Fig. 9(c) represent the reconstructed distributions of the relative dielectric permittivity
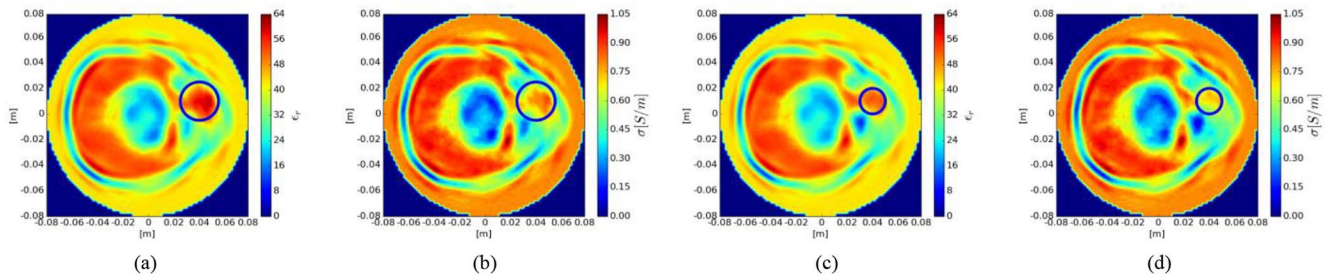
FIGURE 10. Realistic neck configuration with tumor centered in $(0.04, 0.01)$ m. Test case #4, tumor radius $r_t = 1.5$ cm: Reconstructed map of (a) relative dielectric permittivity; (b) electric conductivity. Test case #5, tumor radius $r_t = 1$ cm: Reconstructed map of (c) relative dielectric permittivity; (d) electric conductivity.

TABLE 2. Reconstruction errors for the considered test cases.

Test case	E_{ε_r}	E_σ
#1	0.3082	0.3459
#2	0.3004	0.3446
#3	0.3071	0.3508
#4	0.2987	0.3428
#5	0.3044	0.3470

and electric conductivity, respectively. The tumor is well detected and characterized. Moreover, the external shape of the neck follows the real one, and the vertebral bone is detected. The corresponding actual neck configuration is shown in Fig. 9(b)–(d). In the second tumor-affected case (Test case #3), a smaller tumor is considered, with radius equal to $r_t = 1$ cm. Fig. 9(e)–(g) show the reconstructed dielectric properties, whereas the actual neck properties are reported in Fig. 9(f)–(h). In both test cases, the tumor is centered at $(0.04, -0.01)$ m. The reconstructed maps of the dielectric properties allow the discrimination between the two different tumor sizes, with better results for the relative dielectric permittivity. Furthermore, the external shape of the neck is well reconstructed, as well as its main tissues, *i.e.*, vertebral bone, trachea, spinal cord, and subcutaneous fat. On the other hand, in both cases the infiltrated fat near the vertebral bone in the posterior part of the neck is not identified, possibly due to its sparsity.

To test the ability to discriminate different tumor positions, other two cases are evaluated. Fig. 10(a) and Fig. 10(b) show the reconstructed maps of ε_r and σ, respectively, with radius of tumor equal to $r_t = 1.5$ cm (Test case #4). Fig. 10(c)–(d) present the reconstructions with tumor radius equal to $r_t = 1$ cm (Test case #5). In these two situations, the tumor is centered at $(0.04, 0.01)$ m. Again, the tumor-like inclusion, the vertebral bone and the internal spinal cord are detected, and the trachea is localized in the correct position. The external boundary of the neck follows the expected shape, as well as the subcutaneous fat. As before, the infiltrated fat near the bone is not detected.

In Table 2, the reconstruction errors on relative dielectric permittivity E_{ε_r} and electric conductivity E_σ for each test case are shown. The errors are calculated using (10)-(11) and represent the normalized root mean squared errors on

the relative dielectric permittivity and on the electric conductivity, respectively. As confirmed by the errors, the dielectric reconstructions are more accurate for the relative dielectric permittivity than the electric conductivity. In summary, the reconstructed distributions of the dielectric properties show that, at least in the considered cases, the neural network is able to reconstruct different dimensions of tumor, for the same position, and also to localize it inside the neck.

V. CONCLUSION

A feasibility analysis of a preliminary developed ANN to reconstruct the microwave distribution of dielectric properties of a cross section of the neck starting from scattered electric field data has been presented. A fully-connected neural network, trained with a set of synthetic neck phantoms, is used to accomplish this task. Such phantoms are generated by using a strategy that allows mimicking the distributions of neck tissues in a realistic way, with random variations. A subset of the created phantoms contains circular inclusions to emulate a tumor, with different dimensions and positions. The network parameters are selected after a preliminary analysis of the performance of various architectures, with different numbers of hidden layers and neurons per layer. A performance metric based on the normalized root mean square error, is used to evaluate the reconstruction results. To test the selected network, anatomically realistic numerical phantoms are considered. The results, although preliminary, are promising and show the possibility of detecting the tumor. Moreover, they suggest that ANNs can be effectively used to reconstruct the dielectric and geometric properties of the human neck starting from scattered electric fields. Future works will be aimed at a more comprehensive validation of the approach and at the extension to the full-vector three-dimensional imaging of the neck to further increase the accuracy of the reconstruction. In addition, the explicit inclusion of physical insights into the inversion procedure will be also considered, with the objective of further enhancing results and provide more accurate reconstructions of the different internal neck tissues.

REFERENCES

[1] N. K. Nikolova, *Introduction to Microwave Imaging*. Cambridge, U.K.: Cambridge Univ. Press, 2017.

[2] N. K. Nikolova, "Microwave imaging for breast cancer," *IEEE Microw. Mag.*, vol. 12, no. 7, pp. 78–94, Dec. 2011, doi: 10.1109/MMM.2011.942702.

[3] G. Bellizzi *et al.*, "Optimization of the working conditions for magnetic Nanoparticle-enhanced microwave diagnostics of breast cancer," *IEEE Trans. Biomed. Eng.*, vol. 65, no. 7, pp. 1607–1616, Jul. 2018, doi: 10.1109/TBME.2017.2753846.

[4] O. M. Bucci, G. Bellizzi, S. Costanzo, L. Crocco, G. Di Massa, and R. Scapaticci, "Assessing detection limits in magnetic nanoparticle enhanced microwave imaging," *IEEE Access*, vol. 6, pp. 43192–43202, 2018, doi: 10.1109/ACCESS.2018.2861461.

[5] M. A. Aldhaeebi, K. Alzoubi, T. S. Almoneef, S. M. Bamatraf, H. Attia, and O. M. Ramahi, "Review of microwaves techniques for breast cancer detection," *Sensors*, vol. 20, no. 8, p. 2390, Apr. 2020, doi: 10.3390/s20082390.

[6] S. Hosseinzadegan, A. Fhager, M. Persson, S. D. Geimer, and P. M. Meaney, "Discrete dipole approximation-based microwave tomography for fast breast cancer imaging," *IEEE Trans. Microw. Theory Techn.*, vol. 69, no. 5, pp. 2741–2752, May 2021, doi: 10.1109/TMTT.2021.3060597.

[7] P. H. Tournier *et al.*, "Numerical modeling and high-speed parallel computing: New perspectives on tomographic microwave imaging for brain stroke detection and monitoring," *IEEE Antennas Propag. Mag.*, vol. 59, no. 5, pp. 98–110, Oct. 2017, doi: 10.1109/MAP.2017.2731199.

[8] R. Scapaticci, M. Bjelogrlic, J. A. T. Vasquez, F. Vipiana, M. Mattes, and L. Crocco, "Microwave technology for brain imaging and monitoring: Physical foundations, potential and limitations," in *Emerging Electromagnetic Technologies for Brain Diseases Diagnostics, Monitoring and Therapy*, L. Crocco, I. Karanasiou, M. L. James, and R. C. Conceição, Eds. Cham, Switzerland: Springer Int., 2018, pp. 7–35, doi: 10.1007/978-3-319-75007-1_2.

[9] I. Bisio *et al.*, "Variable-exponent Lebesgue-space inversion for brain stroke microwave imaging," *IEEE Trans. Microw. Theory Techn.*, vol. 68, no. 5, pp. 1882–1895, May 2020, doi: 10.1109/TMTT.2019.2963870.

[10] A. Al-Saffar, A. Bialkowski, M. Baktashmotlagh, A. Trakic, L. Guo, and A. Abbosh, "Closing the gap of simulation to reality in electromagnetic imaging of brain strokes via deep neural networks," *IEEE Trans. Comput. Imag.*, vol. 7, pp. 13–21, Dec. 2021, doi: 10.1109/TCI.2020.3041092.

[11] A. Zakaria, A. Baran, and J. LoVetri, "Estimation and use of prior information in FEM-CSI for biomedical microwave tomography," *IEEE Antennas Wireless Propag. Lett.*, vol. 11, pp. 1606–1609, 2012, doi: 10.1109/LAWP.2012.2237537.

[12] A. Zamani, S. A. Rezaeieh, K. S. Bialkowski, and A. M. Abbosh, "Boundary estimation of imaged object in microwave medical imaging using antenna resonant frequency shift," *IEEE Trans. Antennas Propag.*, vol. 66, no. 2, pp. 927–936, Feb. 2018, doi: 10.1109/TAP.2017.2780898.

[13] C. Dachena, A. Fedeli, A. Fanti, M. B. Lodi, M. Pastorino, and A. Randazzo, "Microwave imaging for the diagnosis of cervical diseases: A feasibility analysis," *IEEE J. Electromagn. RF Microw. Med. Biol.*, vol. 5, no. 3, pp. 277–285, Sep. 2021, doi: 10.1109/JERM.2020.3042711.

[14] M. T. Bevacqua, G. G. Bellizzi, T. Isernia, and L. Crocco, "A method for effective permittivity and conductivity mapping of biological scenarios via segmented contrast source inversion," *Progr. Electromagn. Res.*, vol. 164, pp. 1–15, Nov. 2019, doi: 10.2528/PIER18071704.

[15] O. Fiser, I. Merunka, and J. Vrba, "Numerical feasibility study of new combined hyperthermia system for head and neck region," in *Proc. 47th Eur. Microw. Conf. (EuMC)*, Nuremberg, Germany, Oct. 2017, pp. 719–722, doi: 10.23919/EuMC.2017.8230948.

[16] G. Bellizzi and O. M. Bucci, "Magnetic nanoparticle-guided blind focusing in microwave hyperthermia of neck tumors," *IEEE Access*, vol. 7, pp. 64063–64076, 2019, doi: 10.1109/ACCESS.2019.2916059.

[17] P. Togni *et al.*, "Electromagnetic redesign of the HYPERcollar applicator: Toward improved deep local head-and-neck hyperthermia," *Phys. Med. Biol.*, vol. 58, no. 17, p. 5597, Aug. 2013, doi: 10.1088/0031-9155/58/17/5997.

[18] R. Guo et al., "CT-based radiomics features in the prediction of thyroid cartilage invasion from laryngeal and hypopharyngeal squamous cell carcinoma," *Cancer Imag.*, vol. 20, no. 1, p. 81, Dec. 2020, doi: 10.1186/s40644-020-00359-2.

[19] H. K. Kim, E. J. Ha, M. Han, J. Lee, and E. Y. Soh, "Reoperations for structurally persistent or recurrent disease after thyroidectomy: Analysis via preoperative CT," *Sci. Rep.*, vol. 10, no. 1, Dec. 2020, Art. no. 12376, doi: 10.1038/s41598-020-69398-w.

[20] S. Gao, M. Zheng, X. Ren, Y. Tang, and X. Liang, "Local hyperthermia in head and neck cancer: Mechanism, application and advance," *Oncotarget*, vol. 7, no. 35, pp. 57367–57378, Jun. 2016, doi: 10.18632/oncotarget.10350.

[21] M. M. Paulides, G. M. Verduijn, and N. Van Holthe, "Status quo and directions in deep head and neck hyperthermia," *Radiat. Oncol.*, vol. 11, no. 1, p. 21, Feb. 2016, doi: 10.1186/s13014-016-0588-8.

[22] N. R. Datta, H. P. Kok, H. Crezee, U. S. Gaipl, and S. Bodis, "Integrating loco-regional hyperthermia into the current oncology practice: SWOT and TOWS analyses," *Front. Oncol.*, vol. 10, p. 819, Jun. 2020, doi: 10.3389/fonc.2020.00819.

[23] S.-Y. Lee, G. Fiorentini, A. M. Szasz, G. Szigeti, A. Szasz, and C. A. Minnaar, "Quo vadis oncological hyperthermia (2020)?" *Front. Oncol.*, vol. 10, p. 1690, Sep. 2020, doi: 10.3389/fonc.2020.01690.

[24] H. D. Trefná *et al.*, "Quality assurance guidelines for superficial hyperthermia clinical trials: I. Clinical requirements," *Int. J. Hyperthermia*, vol. 33, no. 4, pp. 471–482, May 2017, doi: 10.1080/02656736.2016.1277791.

[25] H. Dobšíček Trefná *et al.*, "Quality assurance guidelines for superficial hyperthermia clinical trials: II. Technical requirements for heating devices," *Strahlentherapie und Onkologie*, vol. 193, no. 5, pp. 351–366, May 2017, doi: 10.1007/s00066-017-1106-0.

[26] S. Gavazzi *et al.*, "Advanced patient-specific hyperthermia treatment planning," *Int. J. Hyperthermia*, vol. 37, no. 1, pp. 992–1007, Jan. 2020, doi: 10.1080/02656736.2020.1806361.

[27] H. P. Kok *et al.*, "Treatment planning facilitates clinical decision making for hyperthermia treatments," *Int. J. Hyperthermia*, vol. 38, no. 1, pp. 532–551, Jan. 2021, doi: 10.1080/02656736.2021.1903583.

[28] M. Pastorino and A. Randazzo, *Microwave Imaging Methods and Applications*. Boston, MA, USA: Artech House, 2018.

[29] F. Soldovieri and R. Solimene, "Ground penetrating radar subsurface imaging of buried objects," in *Radar Technology*, G. Kouemou, Ed. London, U.K.: IntechOpen, 2010. Accessed: Nov. 9, 2016. [Online]. Available: http://www.intechopen.com/books/radar-technology/ground-penetrating-radar-subsurface-imaging-of-buried-objects

[30] A. Brancaccio and G. Leone, "Multimonostatic shape reconstruction of two-dimensional dielectric cylinders by a Kirchhoff-based approach," *IEEE Trans. Geosci. Remote Sens.*, vol. 48, no. 8, pp. 3152–3161, Aug. 2010, doi: 10.1109/TGRS.2010.2045387.

[31] D. Byrne, M. Sarafianou, and I. J. Craddock, "Compound radar approach for breast imaging," *IEEE Trans. Biomed. Eng.*, vol. 64, no. 1, pp. 40–51, Jan. 2017, doi: 10.1109/TBME.2016.2536703.

[32] M. Ambrosanio, M. T. Bevacqua, T. Isernia, and V. Pascazio, "Performance analysis of tomographic methods against experimental contactless multistatic ground penetrating radar," *IEEE J. Sel. Topics Appl. Earth Observ. Remote Sens.*, vol. 14, pp. 1171–1183, Oct. 2021, doi: 10.1109/JSTARS.2020.3034996.

[33] G. Oliveri, L. Lizzi, M. Pastorino, and A. Massa, "A nested multi-scaling inexact-Newton iterative approach for microwave imaging," *IEEE Trans. Antennas Propag.*, vol. 60, no. 2, pp. 971–983, Feb. 2012, doi: 10.1109/TAP.2011.2173131.

[34] C. Estatico, A. Fedeli, M. Pastorino, and A. Randazzo, "Microwave imaging by means of Lebesgue-space inversion: An overview," *Electronics*, vol. 8, no. 9, p. 945, Sep. 2019, doi: 10.3390/electronics8090945.

[35] N. Abdollahi, I. Jeffrey, and J. LoVetri, "Improved tumor detection via quantitative microwave breast imaging using eigenfunction-based prior," *IEEE Trans. Comput. Imag.*, vol. 6, pp. 1194–1202, Jul. 2020, doi: 10.1109/TCI.2020.3012940.

[36] C. Estatico, A. Fedeli, M. Pastorino, A. Randazzo, and E. Tavanti, "A phaseless microwave imaging approach based on a Lebesgue-space inversion algorithm," *IEEE Trans. Antennas Propag.*, vol. 68, no. 12, pp. 8091–8103, Dec. 2020, doi: 10.1109/TAP.2020.2999789.

[37] N. Bayat and P. Mojabi, "A multiplicative regularizer augmented with spatial priors for microwave imaging," *IEEE Trans. Antennas Propag.*, vol. 69, no. 1, pp. 606–611, Jan. 2021, doi: 10.1109/TAP.2020.2998913.

[38] A. Fedeli, V. Schenone, A. Randazzo, M. Pastorino, T. Henriksson, and S. Semenov, "Nonlinear S-parameters inversion for stroke imaging," *IEEE Trans. Microw. Theory Techn.*, vol. 69, no. 3, pp. 1760–1771, Mar. 2021, doi: 10.1109/TMTT.2020.3040483.

[39] I. T. Rekanos, "Inverse scattering of dielectric cylinders by using radial basis function neural networks," *Radio Sci.*, vol. 36, no. 5, pp. 841–849, Sep./Oct. 2001, doi: 10.1029/2000RS002545.

[40] E. Bermani, S. Caorsi, and M. Raffetto, "An inverse scattering approach based on a neural network technique for the detection of dielectric cylinders buried in a lossy half-space," *Progr. Electromagn. Res.*, vol. 26, pp. 67–87, Jan. 2000, doi: 10.2528/PIER99052001.

[41] W. Shao and Y. Du, "Microwave imaging by deep learning network: Feasibility and training method," *IEEE Trans. Antennas Propag.*, vol. 68, no. 7, pp. 5626–5635, Jul. 2020, doi: 10.1109/TAP.2020.2978952.

[42] A. Yago, M. Cavagnaro, and L. Crocco, "Deep learning-enhanced qualitative microwave imaging: Rationale and initial assessment," in *Proc. 15th Eur. Conf. Antennas Propag. (EuCAP)*, Dusseldorf, Germany, Mar. 2021, pp. 1–5, doi: 10.23919/EuCAP51087.2021.9411361.

[43] Y. Huang, R. Song, K. Xu, X. Ye, C. Li, and X. Chen, "Deep learning-based inverse scattering with structural similarity loss functions," *IEEE Sensors J.*, vol. 21, no. 4, pp. 4900–4907, Feb. 2021, doi: 10.1109/JSEN.2020.3030321.

[44] H. M. Yao, L. Jiang, and W. E. I. Sha, "Enhanced deep learning approach based on the deep convolutional encoder–decoder architecture for electromagnetic inverse scattering problems," *IEEE Antennas Wireless Propag. Lett.*, vol. 19, no. 7, pp. 1211–1215, Jul. 2020, doi: 10.1109/LAWP.2020.2995455.

[45] L. Zhang, K. Xu, R. Song, X. Ye, G. Wang, and X. Chen, "Learning-based quantitative microwave imaging with a hybrid input scheme," *IEEE Sensors J.*, vol. 20, no. 24, pp. 15007–15013, Dec. 2020, doi: 10.1109/JSEN.2020.3012177.

[46] S. D. Campbell, R. P. Jenkins, P. J. O'Connor, and D. Werner, "The explosion of artificial intelligence in antennas and propagation: How deep learning is advancing our state of the art," *IEEE Antennas Propag. Mag.*, vol. 63, no. 3, pp. 16–27, Jun. 2021, doi: 10.1109/MAP.2020.3021433.

[47] M. Li *et al.*, "Machine learning in electromagnetics with applications to biomedical imaging: A review," *IEEE Antennas Propag. Mag.*, vol. 63, no. 3, pp. 39–51, Jun. 2021, doi: 10.1109/MAP.2020.3043469.

[48] O. Ronneberger, P. Fischer, and T. Brox, "U-Net: Convolutional networks for biomedical image segmentation," in *Medical Image Computing and Computer-Assisted Intervention (MICCAI)*, vol. 9351, N. Navab, J. Hornegger, W. M. Wells, and A. F. Frangi, Eds. Cham, Switzerland: Springer Int., 2015, pp. 234–241, doi: 10.1007/978-3-319-24574-4_28.

[49] K. He, X. Zhang, S. Ren, and J. Sun, "Deep residual learning for image recognition," in *Proc. IEEE Conf. Comput. Vis. Pattern Recognit. (CVPR)*, Las Vegas, NV, USA, Jun. 2016, pp. 770–778, doi: 10.1109/CVPR.2016.90.

[50] K. Simonyan and A. Zisserman, "Very deep convolutional networks for large-scale image recognition," Apr. 2015. Accessed: Aug. 6, 2021. [Online]. Available: http://arxiv.org/abs/1409.1556.

[51] Z. Wei and X. Chen, "Physics-inspired convolutional neural network for solving full-wave inverse scattering problems," *IEEE Trans. Antennas Propag.*, vol. 67, no. 9, pp. 6138–6148, Sep. 2019, doi: 10.1109/TAP.2019.2922779.

[52] Z. Wei and X. Chen, "Deep-learning schemes for full-wave nonlinear inverse scattering problems," *IEEE Trans. Geosci. Remote Sens.*, vol. 57, no. 4, pp. 1849–1860, Apr. 2019, doi: 10.1109/TGRS.2018.2869221.

[53] S. Franceschini, M. Ambrosanio, F. Baselice, and V. Pascazio, "Neural networks for inverse problems: The microwave imaging case," in *Proc. 15th Eur. Conf. Antennas Propag. (EuCAP)*, Dusseldorf, Germany, Mar. 2021, pp. 1–5, doi: 10.23919/EuCAP51087.2021.9411317.

[54] H. M. Yao, W. E. I. Sha, and L. Jiang, "Two-step enhanced deep learning approach for electromagnetic inverse scattering problems," *IEEE Antennas Wireless Propag. Lett.*, vol. 18, no. 11, pp. 2254–2258, Nov. 2019, doi: 10.1109/LAWP.2019.2925578.

[55] M. T. Bevacqua, T. Isernia, R. Palmeri, M. N. Akinci, and L. Crocco, "Physical insight unveils new imaging capabilities of orthogonality sampling method," *IEEE Trans. Antennas Propag.*, vol. 68, no. 5, pp. 4014–4021, May 2020, doi: 10.1109/TAP.2019.2963229.

[56] K. Belkebir, P. C. Chaumet, and A. Sentenac, "Superresolution in total internal reflection tomography," *J. Opt. Soc. Amer. A*, vol. 22, no. 9, pp. 1889–1897, Sep. 2005, doi: 10.1364/JOSAA.22.001889.

[57] S.-H. Son, K.-J. Lee, and W.-K. Park, "Application and analysis of direct sampling method in real-world microwave imaging," *Appl. Math. Lett.*, vol. 96, pp. 47–53, Oct. 2019, doi: 10.1016/j.aml.2019.04.016.

[58] P. M. Meaney, K. D. Paulsen, S. D. Geimer, S. A. Haider, and M. W. Fanning, "Quantification of 3-D field effects during 2-D microwave imaging," *IEEE Trans. Biomed. Eng.*, vol. 49, no. 7, pp. 708–720, Jul. 2002, doi: 10.1109/TBME.2002.1010855.

[59] A. F. Agarap, "Deep learning using rectified linear units (ReLU)," Feb. 2019. Accessed: Aug. 22, 2021. [Online]. Available: http://arxiv.org/abs/1803.08375.

[60] D. P. Kingma and J. Ba, "Adam: A method for stochastic optimization," Jan. 2017. Accessed: Apr. 19, 2021. [Online]. Available: http://arxiv.org/abs/1412.6980.

[61] L. Li, L. G. Wang, F. L. Teixeira, C. Liu, A. Nehorai, and T. J. Cui, "DeepNIS: Deep neural network for nonlinear electromagnetic inverse scattering," *IEEE Trans. Antennas Propag.*, vol. 67, no. 3, pp. 1819–1825, Mar. 2019, doi: 10.1109/TAP.2018.2885437.

[62] A. Christ et al., "The Virtual family—Development of surface-based anatomical models of two adults and two children for dosimetric simulations," *Phys. Med. Biol.*, vol. 55, no. 2, p. N23, Jan. 2010, doi: 10.1088/0031-9155/55/2/N01.

[63] S. Gabriel, R. W. Lau, and C. Gabriel, "The dielectric properties of biological tissues: III. Parametric models for the dielectric spectrum of tissues," *Phys. Med. Biol.*, vol. 41, no. 11, p. 2271, Nov. 1996, doi: 10.1088/0031-9155/41/11/003.

[64] A. Ruggeri, "Development and multiphysic analysis of a neck phantom for microwave hyperthermia," in *Proc. 28th Telecommun. Forum (TELFOR)*, Nov. 2020, pp. 1–4, doi: 10.1109/TELFOR51502.2020.9306679.

[65] M. M. Paulides *et al.*, "The HYPERcollar: A novel applicator for hyperthermia in the head and neck," *Int. J. Hyperthermia*, vol. 23, no. 7, pp. 567–576, Jan. 2007, doi: 10.1080/02656730701670478.

[66] R. Gaffoglio, M. Righero, G. Giordanengo, M. Zucchi, and G. Vecchi, "Fast optimization of temperature focusing in hyperthermia treatment of sub-superficial tumors," *IEEE J. Electromagn. RF Microw. Med. Biol.*, vol. 5, no. 3, pp. 286–293, Sep. 2021, doi: 10.1109/JERM.2020.3043383.

[67] M. Zanoli and H. D. Trefná, "Iterative time-reversal for multi-frequency hyperthermia," *Phys. Med. Biol.*, vol. 66, no. 4, Feb. 2021, Art. no. 045027, doi: 10.1088/1361-6560/abd41a.

[68] L. Hadjiiski *et al.*, "Treatment response assessment of head and neck cancers on CT using computerized volume analysis," *Amer. J. Neuroradiol.*, vol. 31, no. 9, pp. 1744–1751, Oct. 2010, doi: 10.3174/ajnr.A2177.

[69] N. Tong, S. Gou, S. Yang, D. Ruan, and K. Sheng, "Fully automatic multi-organ segmentation for head and neck cancer radiotherapy using shape representation model constrained fully convolutional neural networks," *Med. Phys.*, vol. 45, no. 10, pp. 4558–4567, 2018, doi: 10.1002/mp.13147.

[70] J. Y. Lim and M. Leech, "Use of auto-segmentation in the delineation of target volumes and organs at risk in head and neck," *Acta Oncol.*, vol. 55, no. 7, pp. 799–806, Jul. 2016, doi: 10.3109/0284186X.2016.1173723.

[71] R. Bartels, J. Beatty, and B. Barsky, *An Introduction to Splines for Use in Computer Graphics and Geometric Modeling*. San Mateo, CA, USA: Morgan Kaufmann, 1995.

[72] M. Zamani, "A simple 2D interpolation model for analysis of nonlinear data," *Nat. Sci.*, vol. 2, no. 6, pp. 641–645, Jun. 2010, doi: 10.4236/ns.2010.26080.

[73] T. Drizdal, M. M. Paulides, N. van Holthe, and G. C. van Rhoon, "Hyperthermia treatment planning guided applicator selection for sub-superficial head and neck tumors heating," *Int. J. Hyperthermia*, vol. 34, no. 6, pp. 704–713, Aug. 2018, doi: 10.1080/02656736.2017.1383517.

CHIARA DACHENA received the bachelor's degree in biomedical engineering from the University of Cagliari, Cagliari, in 2017, and the master's degree in bioengineering from the University of Genoa, Genoa, Italy, in 2019, where she is currently pursuing the Ph.D. degree in science and technology for electronic and telecommunications engineering. Her research activity deals with microwave imaging for biomedical applications, inversion procedure of scattering problems, and application of machine learning for electromagnetic problems.

ALESSANDRO FEDELI (Member, IEEE) received the B.Sc. and M.Sc. degrees in electronic engineering and the Ph.D. degree in science and technology for electronic and telecommunications engineering from the University of Genoa, Genoa, Italy, in 2011, 2013, and 2017, respectively, where he is currently an Assistant Professor with the Department of Electrical, Electronic, Telecommunications Engineering, and Naval Architecture. His research activities, carried out at the Applied Electromagnetics Laboratory, are mainly focused on the development and the application of computational methods for the solution of forward and inverse scattering problems, and electromagnetic imaging. He has coauthored more than 130 scientific contributions published in international journals and conference proceedings. He is a member of the IEEE Antennas and Propagation Society, the Italian Society of Electromagnetism, and the Interuniversity Center for the Interaction between Electromagnetic Fields and Biosystems.

ALESSANDRO FANTI (Member, IEEE) received the Laurea degree in electronic engineering and Ph.D. degree in electronic engineering and computer science from the University of Cagliari, Cagliari, Italy, in 2006 and 2012, respectively. He worked as a Postdoctoral Fellow of the Electromagnetic Group, University of Cagliari from 2013 to 2016, where he is currently an Assistant Professor. Since 2016, he has been a Scientific Associate with INFN (National Institute of Nuclear Physics–Cagliari division). His research activity involves the use of numerical techniques for modes computation of guiding structures, optimization techniques, analysis and design of waveguide slot arrays, analysis and design of patch antennas, radio propagation in urban environment, modeling of bioelectromagnetic phenomena, and microwave exposure systems for biotechnology and bioagriculture. He is an Associate Editor of the IEEE JOURNAL OF ELECTROMAGNETICS, RF AND MICROWAVES IN MEDICINE AND BIOLOGY. From 2020 to 2023, he acts as a Principal Investigator of the "IAPC" Project, funded with € 5 million by the Italian Ministry of Economic Development (MISE), within the AGRIFOOD PON I&C 2014-2020 (CUP: B21B1900064008 COR: 1406652).
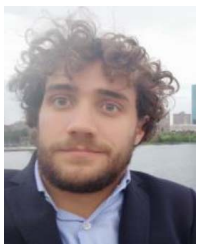
MATTEO BRUNO LODI (Graduate Student Member, IEEE) received the bachelor's degree in biomedical engineering from the University of Cagliari, Cagliari, in 2016, and the master's degree in biomedical engineering from the Politecnico di Torino, Turin, Italy, in 2018. He is currently pursuing the Ph.D. degree in electronic engineering and computer science with the University of Cagliari. His research activity deals with the modeling of bioelectromagnetic phenomena, especially hyperthermia treatment; the study, manufacturing, and synthesis of magnetic biomaterials for tissue engineering applications; and the use of microwave for biotechnology and environmental applications. He was awarded as a Young Scientists at General Assembly and Scientific Symposium of URSI 2020 and 2021. He has been appointed as a Representative for the Young Professionals of IEEE Region 8 Nanotechnology Council. He is a member of the Editorial Board of the IEEE Future Directions Technology Policy and Ethics newsletter.

GIORGIO FUMERA (Member, IEEE) received the Ph.D. degree in electronic engineering and computer science from the University of Cagliari, Italy, in 2002, where he has been an Associate Professor of Computer Engineering Since 2010. His research interests are related to methodologies and applications of statistical pattern recognition, and include multiple classifier systems, adversarial machine learning, and computer vision for intelligent video surveillance. He is Associate Editor of the *Pattern Recognition* and the *Pattern Analysis and Applications* journals.

ANDREA RANDAZZO (Senior Member, IEEE) received the Laurea degree in telecommunication engineering and the Ph.D. degree in information and communication technologies from the University of Genoa, Genoa, Italy, in 2001 and 2006, respectively. He is currently a Full Professor of electromagnetic fields with the Department of Electrical, Electronic, Telecommunication Engineering, and Naval Architecture, University of Genoa. He has coauthored the book *Microwave Imaging Methods and Applications* (Artech House, 2018) and more than 270 articles published in journals and conference proceedings. His primary research interests are in the field of microwave imaging, inverse-scattering techniques, numerical methods for electromagnetic scattering and propagation, electrical tomography, and smart antennas.

MATTEO PASTORINO (Fellow, IEEE) is a Full Professor of electromagnetic fields with the University of Genoa, Genoa, Italy, where he is the Director of the Department of Electrical, Electronic, Telecommunications Engineering, and Naval Architecture (DITEN). He has coauthored about 500 articles in international journals and conference proceedings. His research interests include microwave and millimeter wave imaging, direct and inverse scattering problems, industrial and medical applications, smart antennas, and analytical and numerical methods in electromagnetism.

Prof. Pastorino is the Chair of the National URSI Commission B (Fields and Waves) the Vice Director of the Interuniversity Center for the Interaction between Electromagnetic Fields and Biosystems. He is an Associate Editor of the *IEEE Antennas and Propagation Magazine* and the IEEE OPEN JOURNAL OF ANTENNAS AND PROPAGATION.